Biophysical Journal Volume 81 August 2001 799–813

# Multiparticle Adhesive Dynamics. Interactions between Stably Rolling Cells

Michael R. King and Daniel A. Hammer
Departments of Chemical Engineering and Bioengineering and Institute for Medicine and Engineering, University of Pennsylvania,
Philadelphia, Pennsylvania 19104 USA

ABSTRACT A novel numerical simulation of adhesive particles (cells) reversibly interacting with an adhesive surface under flow is presented. Particle–particle and particle–wall hydrodynamic interactions in low Reynolds number Couette flow are calculated using a boundary element method that solves an integral representation of the Stokes equation. Molecular bonds between surfaces are modeled as linear springs and stochastically formed and broken according to postulated descriptions of force-dependent kinetics. The resulting simulation, Multiparticle Adhesive Dynamics, is applied to the problem of selectin-mediated rolling of hard spheres coated with leukocyte adhesion molecules (cell-free system). Simulation results are compared to flow chamber experiments performed with carbohydrate-coated spherical beads rolling on P-selectin. Good agreement is found between theory and experiment, with the main observation being a decrease in rolling velocity with increasing concentration of rolling cells or increasing proximity between rolling cells. Pause times are found to increase and deviation motion is found to decrease as pairs of rolling cells become closer together or align with the flow.

## INTRODUCTION

The adhesion of cells with surfaces in the microvasculature is important in the inflammatory response, lymphocyte homing to lymphatic tissues, and stem cell homing (Bevilacqua et al., 1994; Lasky, 1995; Ebnet and Vestweber, 1999). A key step in these adhesive interactions is rolling, in which the adhesion of cells to surfaces slows, but does not stop, the motion of a cell under hydrodynamic flow. Initial adhesive contact is mediated by the selectin family of molecules and their ligands: P- and E-selectin and peripheral node addressin expressed on the surface of endothelial cells, and L-selectin or P-selectin glycoprotein-1 (PSGL-1), which is found at the tips of leukocyte microvilli. Flow chamber experiments with leukocytes perfused over an isolated species of adhesion molecule have identified the role of selectin-mediated rolling as a necessary precursor to integrin-mediated firm adhesion of leukocytes (Lawrence and Springer, 1991). Also, studies in double knockout mice show that deficiency in E- and P-selectin can eliminate the cellular inflammatory response, even when integrins and their ligands are available for firm adhesion; thus, selectin-mediated rolling is critical for inflammation (Bullard et al., 1996). Many of the receptors and counterreceptors involved in leukocyte homing and recirculation have been identified (Ebnet and Vestweber, 1999). Demonstration that rolling is due to selectin–ligand physical chemistry has come from reconstitution of selectin ligands on colloidal spheres; these spheres readily roll over selectin-coated surfaces. These synthetic model cells reproduce the essential features of leukocyte rolling in vivo: the inherent noisiness of rolling velocity, the dependence of average velocity on molecular density on either surface, and shear rate dependence (Brunk et al., 1996; Brunk and Hammer, 1997; Rodgers et al., 2000; Greenberg et al., 2000). The cell-free system represents a means of systematically varying system parameters, such as molecular density or chemistry, to study the biophysics of adhesion.

Most rolling experiments, and all cell-free rolling experiments thus far, have been performed using very dilute suspensions of cells or beads (<0.1% by volume) in buffer solution. This stands in contrast to physiologic conditions where erythrocytes comprise 20–40% of the blood by volume, and leukocytes are found at relatively high concentrations near the vessel walls (Goldsmith and Spain, 1984). Indeed, in vivo observations of cell rolling show differences with in vitro leukocyte and cell-free flow chamber experiments performed at low density. Stable rolling in vivo is found to persist at much higher shear rates than is seen in vitro (Bullard et al., 1996), and the motion is smoother and with fewer pauses (Damiano et al., 1996). It is often unclear whether such differences are due to leukocyte rheology, flow geometry, or locally varying levels of selectin expression. Recent work has examined the effect erythrocytes have on rolling dynamics both in vitro (Munn et al., 1996) and in mouse models (Melder et al., 2000). Data show an increase in the number of rolling leukocytes with increasing hematocrit, perhaps due to an increase in the near wall concentration of leukocytes or due to collision-induced contact of the cells with the reactive surface.

To better understand the relationship between the molecular properties of adhesive receptor/ligand interactions and the macroscopic behavior such as rolling or firm adhesion that they mediate, Hammer and Apte (1992) devised a direct numerical simulation of a spherical cell interacting with a reactive surface under flow. Their

---

*Received for publication 5 March 2001 and in final form 9 May 2001.*

Address reprint requests to Daniel A. Hammer, Department of Bioengineering, University of Pennsylvania, 120 Hayden Hall, 3320 Smith Walk, Philadelphia, PA 19104. Tel.: 215-573-6761; Fax: 215-573-2071; E-mail: hammer@seas.upenn.edu.

0006-3495/01/08/799/15 $2.00

model incorporates the hydrodynamics of a sphere rotating and translating near a plane under shear flow (Jeffrey, 1915; Brenner, 1961; Goldman et al., 1967a,b), and the force-dependent binding kinetics proposed by Bell (1978) and later modified by Dembo and coworkers (Dembo et al., 1988). A Monte Carlo simulation of the molecular binding and unbinding events is coupled with the deterministic solution of the equations of cell motion, which include hydrodynamics and wall effects. Later work demonstrated that the adhesive dynamics (AD) simulation accurately reproduces the fine scale dynamics of selectin-mediated rolling (Chang and Hammer, 2000), and, given information on the physical chemistry of a receptor–ligand pair, the simulation can predict the dynamic behavior of cells contacting surfaces under shear flow (Chang et al., 2000).

A severe limitation for the applicability of this theoretical work to adhesion in dense systems (i.e., blood) is that, to date, there has been no attempt to model the effect of particle–particle (cell–cell) hydrodynamic interactions on the dynamics of cell adhesion. The goal is to incorporate these interactions while preserving the rigor of AD for modeling cell adhesion to surfaces. The purpose of this paper is to present a novel numerical simulation of multiparticle cell rolling that serves to combine particle–particle interactions with AD. Corresponding cell-free experiments have been performed specifically to test the simulation and demonstrate how additional insight into physiologic rolling phenomena may be gained by consideration of hydrodynamic particle–particle interactions. The next section reviews the computational technique, outlines the hydrodynamic calculation used to determine cell motions, and summarizes the experimental methods. Results from the simulation and experiments are then presented and compared. Finally, we comment on some recent experimental visualizations of leukocyte rolling where hydrodynamic interactions may be important, and then summarize our findings.

## METHODS

### Adhesive dynamics

The AD algorithm has been thoroughly described in several articles by Hammer and coworkers (Hammer and Apte, 1992; Chang and Hammer, 2000; Chang et al., 2000). Essentially, a large number of adhesion molecules are randomly placed on the surface of a sphere and bounding wall. In the near-contact region between sphere and plane, adhesive receptor–ligand pairs are randomly tested for bond formation according to their deviation length-dependent binding kinetics. If a bond forms, over its lifetime it is represented by a linear spring whose endpoints remain fixed with respect to either surface. The orientation and length of each spring specifies the instantaneous force and torque exerted by that bond on the sphere, and also its probability for breakage per unit time. A summation of all external forces and torques enables a mobility calculation to determine the translational and rotational velocities of the sphere under flow. For a single particle in low Reynolds number Couette flow, the mobility function is available as a closed-form solution for all modes of motion (Hammer and Apte, 1992).

One model commonly used to describe the kinetics of single biomolecular bond failure is that of Bell (1978),

$$k_{\mathrm{r}} = k_{\mathrm{r}}^{0} exp\left[\frac{r_0 F}{k_{\mathrm{b}} T}\right], \tag{1}$$

which relates the rate of dissociation $k_{\mathrm{r}}$ to the magnitude of the force on the bond $F$. The unstressed off-rate $k_{\mathrm{r}}^{0}$ and reactive compliance $r_0$ have been experimentally determined for the selectins with their respective ligands by observing pause-time distributions when perfusing cells or beads over sparsely populated surfaces (Alon et al., 1995; Smith et al., 1999). Other more sophisticated methods, collectively known as dynamic force microscopy (Evans and Ritchie, 1997; Tees et al., 2001), have been used to measure the force-driven dissociation of single bonds, demonstrating that the Bell equation is valid over some force loading regimes (typically fast loading). Once the rate of dissociation is known, the rate of formation directly follows from the Boltzmann distribution for affinity (Bell et al., 1984),

$$\frac{k_{\mathrm{f}}}{k_{\mathrm{r}}} = \frac{k_{\mathrm{f}}^{0}}{k_{\mathrm{r}}^{0}} \exp\left[\frac{-\sigma|\mathbf{x}_{\mathrm{b}} - \lambda|^{2}}{2k_{\mathrm{b}}T}\right], \tag{2}$$

and takes the form

$$k_{\mathrm{f}} = k_{\mathrm{f}}^{0} exp[\sigma|\mathbf{x}_{\mathrm{b}} - \lambda|(r_0 - \tfrac{1}{2}|\mathbf{x}_{\mathrm{b}} - \lambda|)/k_{\mathrm{b}}T]. \tag{3}$$

In the above expressions, $\sigma$ is the Hookean spring constant and $|\mathbf{x}_{\mathrm{b}} - \lambda|$ is the deviation bond length. The intrinsic on-rate $k_{\mathrm{f}}^{0}$ has not been adequately measured and is adjusted for a selectin–ligand species to match the simulations with experiment. This expression for the forward binding rate must also incorporate the effect of the relative motion of the two surfaces. Chang and Hammer (1999) calculated the effective rate of collision of surface-tethered reactants in relative motion when the Peclet number (Pe = (radius of receptor)(relative velocity)/(lateral diffusivity)) is nonzero, and showed that the on-rate exhibits a first-order dependence on Pe. The result is that the probability of bond formation is proportional to the slip velocity between the cell and plane, which has important implications to both commonly observed phenomena such as the shear-threshold effect (Finger et al., 1996; Greenberg et al., 2000) and the present study.

A very short-range repulsive force representing the contact force between surfaces is included, of the form

$$F_{\mathrm{rep}} = F_0 \frac{\tau e^{-\tau\epsilon}}{1 - e^{-\tau\epsilon}}, \tag{4}$$

where $1/\tau$ is a length scale on the order of angstroms and $\epsilon$ is the surface-to-surface separation. $F_{\mathrm{rep}}$ is directed normal to the plane in the case of cell–plane interactions. In the presence of particle–particle interactions, Eq. 4 is also used, directed along the line connecting cell centers. Although these two parameters have a physical significance when Eq. 4 is used as a model of the repulsion of an electronic double layer (Takamura et al., 1981), we use Eq. 4 as a generic short-range interaction and arbitrarily assign values of $\tau = 5$ Å and $F_0 = 10^3$ N. This force is of sufficiently short range to allow specific chemical adhesion while preventing cell overlap. Phenomenological expressions of this mathematical form have been used in other studies of cell adhesion, where ions in solution filter out the longer range van der Waals attraction (Bell et al., 1984). As a model of the roughness of the spherical and planar surfaces, it was assumed that both surfaces are covered with small bumps of sufficient coverage to support the particle, yet of a dilution that permits the flow disturbance caused by the bumps to be neglected. The contact interactions of adhesion and repulsion are exerted by the tips of these roughness elements. This simple model of surface roughness serves as a steric layer that prevents the hydrodynamic lubrication singularity that would be created by a mathematically smooth sphere contacting a mathematically smooth plane, a physically unrealistic situation. A value of surface roughness consistent with scanning electron micrographs of the beads was used, and, in practice, the results were found to be insensitive to the precise value of this parameter. Gravitational force is added, because beads and cells are typically denser than aqueous solution. This force promotes initial contact between the cell and the wall.

The solution algorithm for single cell AD is as follows: (1) all unbound molecules in the contact area are tested for formation against the probability $P_f = 1 - \exp(-k_f\Delta t)$, with $k_f$ given by Eq. 3; (2) all of the currently bound molecules are tested for breakage against the probability $P_r = 1 - \exp(-k_r\Delta t)$, with $k_r$ given by Eq. 1; (3) the external forces and torques on each cell are calculated by summing over adhesive forces and adding nonspecific interparticle and gravitational forces; (4) the mobility calculation is performed to determine the rigid body motions of the cells; and (5) cell and bond positions are updated according to the kinematics of cell motion. A MIPSpro Fortran 90 random number generator is used in steps 1 and 2.

An improvement over the original algorithm (Hammer and Apte, 1992) that we have implemented is to only assign coordinates to molecules after they form a bond, and to cease to keep track of these coordinates after the bond has broken. This eliminates the need to continually update the coordinates of unbound molecules, relieving demands on storage and computational time. The contact area is defined as a circular area whose outer radius represents a surface-to-surface separation at which the probability for bond formation becomes vanishingly small. At each time step, the unbound molecules in the contact area are randomly assigned a bond length to perform the Monte Carlo test for bond formation. Note that the proper area weighted distribution of bond lengths is the square root of a uniform random variate ranging from 0 to 1. If the test for formation is successful, then the new bond is given three-dimensional coordinates on both surfaces. Bonds are assumed to be aligned vertically upon formation, a reasonable simplification because extensive calculations have shown that rolling behavior is insensitive to initial bond orientation, and given the small ratio of bond length to particle size. An additional random number, representing the polar angle of the bond in the circular contact area, fixes the coordinates on both surfaces. Because the vast majority of tests result in no new bond formation, this reduces the number of random numbers generated in this formulation.

For small particles suspended in a viscous fluid, one can neglect inertia, and the motion of the fluid is governed by the Stokes and continuity equations,

$$-\nabla p + \mu\nabla^2\mathbf{u} = 0, \quad \nabla\cdot\mathbf{u} = 0. \tag{5}$$

The symbol $p$ denotes the pressure, $\mathbf{u}$ is the velocity, and $\mu$ the fluid viscosity. No-slip conditions are enforced at the surface of each of the $N$ cells:

$$\mathbf{u} = \mathbf{U}_\alpha + \boldsymbol{\omega}_\alpha \times (\mathbf{x} - \mathbf{x}_\alpha) \quad \mathbf{x} \in S_\alpha, \tag{6}$$

where $\mathbf{U}_\alpha$ and $\boldsymbol{\omega}_\alpha$ are the translational and rotational velocities of cell $\alpha$, $\mathbf{x}_\alpha$ its center of mass, and $S_\alpha$ its corresponding surface. The fluid velocity is also taken to be zero at the bounding planar wall ($x_3 = 0$). The motion of an isolated cell is related to the forces acting on it by the 6 × 6 mobility matrix $\mathbf{M}$:

$$\mathbf{u} = \mathbf{M}\mathbf{f}, \tag{7}$$

where $\mathbf{u}$ is a six-element vector containing the sphere's translational and rotational velocities, and $\mathbf{f}$ is a vector containing the three components of net force and three components of the net torque acting on the sphere. For an isolated sphere near a plane in Stokes flow, all of the components of the mobility matrix $\mathbf{M}$ are known (Jeffrey, 1915; Brenner, 1961; Goldman et al., 1967a,b). Thus, after all of the external forces acting on the cell have been summed, the instantaneous sphere velocities can be evaluated directly from Eq. 7.

Although this formalism works well for single-cell hydrodynamics, difficulties arise when extending the technique to $N$ cells. In general, the mobility matrix for an arbitrary number of cells is $6N \times 6N$ in size, but it cannot be explicitly constructed from analytic expressions because the mobility of each cell depends on the position of all others in the fluid. Each cell's translational and rotational motion transmits force on all of the other surfaces through the fluid, coupling all cell velocities in a nonlinear manner. This represents the inherent difficulty in computing particulate flows, where the particle interactions are not simply pairwise.

## Multiparticle mobility calculation

There are several methods now available to simulate the motion of rigid particles suspended in a viscous fluid. Pozrikidis (1999) reviews these different approaches. The Stokesian dynamics method (Brady and Bossis, 1988) is based on inverting a matrix containing the pairwise resistance interactions (from the inverse problem $\mathbf{f} = \mathbf{R}\mathbf{u}$) to yield the full set of multiparticle mobility relations. Recent work has overcome the $O(N^3)$ demands on computational time with an $O(N\log(N))$ formulation (Higdon and Viera, 2000), but Stokesian dynamics remains best suited for the study of large collections of rigid spheres. The other main class of simulation techniques is boundary element solutions of an integral representation of the Stokes equation. The method used in this study, chosen for its applicability to irregularly shaped or deformable bodies, falls into this category.

The development here follows that of Phan-Thien et al. (1992). For a more complete discussion of the derivations and proofs of the completed double layer-boundary integral equation method (CDL-BIEM) the reader is referred to Kim and Karrila (1991). The integral representation of the Stokes equation is

$$u_j(\mathbf{X}) + \int_S H_{ij}(\mathbf{x},\mathbf{X})u_i(\mathbf{x})\,dS(\mathbf{x}) = \int_S G_{ij}(\mathbf{x},\mathbf{X})t_i(\mathbf{x})\,dS(\mathbf{x}), \tag{8}$$

where $G_{ij}(\mathbf{x},\mathbf{X})$ is the singularity solution resulting from a point force in the vicinity of a plane at $\mathbf{x}$ in the $j$th direction, $t_i(\mathbf{x}) = \sigma_{ki}n_k$ is the traction vector at $\mathbf{x}$, $\mathbf{n}$ is the outwardly directed unit normal on $S$, and $H_{ij}(\mathbf{x},\mathbf{X})$ is the associated traction vector of $G_{ij}(\mathbf{x},\mathbf{X})$. In terms of the associated stress obtained from the singularity solution, $\Sigma_{ijk}(\mathbf{x},\mathbf{X})$,

$$H_{ij}(\mathbf{x},\mathbf{X}) = n_k(\mathbf{x})\sum\nolimits_{ijk}(\mathbf{x},\mathbf{X}). \tag{9}$$

In analogy with potential theory, the integral on the right-hand side of Eq. 8 is called the single-layer potential, and the integral on the left-hand side is called the double-layer potential. Inclusion of the single-layer term produces a problem that is, in general, ill-conditioned. To deal with this, we discard the single-layer integral (see justification below) and write an integral representation of the velocity field where only the double layer is retained,

$$u_j(\mathbf{X}) = \int_S K_{ij}(\mathbf{x},\mathbf{X})\phi_i(\mathbf{x})\,dS(\mathbf{x}). \tag{10}$$

The double-layer kernal $K_{ij}$ is given by

$$K_{ij}(\mathbf{x},\mathbf{X}) = 2\hat{n}_k(\mathbf{x})\sum\nolimits_{ijk}(\mathbf{x},\mathbf{X}), \tag{11}$$

where $\hat{\mathbf{n}} = -\mathbf{n}$ is the unit normal vector directed into the fluid and $\phi_i$ in Eq. 10 represents the unknown surface density of the double-layer distribution. The factor of 2 causes the eigenvalues of the double-layer operator to lie within the range $[-1, +1]$. The jump in the velocity field produced by this double-layer distribution appears explicitly when Eq. 10 is evaluated at the cell surface:

$$u_{\mathrm{j}}(\boldsymbol{\zeta}) = \phi_{\mathrm{j}}(\boldsymbol{\zeta}) + \int_{\mathrm{S}} K_{\mathrm{ij}}(\mathbf{x}, \boldsymbol{\zeta})\phi_{\mathrm{i}}(\mathbf{x})\, \mathrm{d}S(\mathbf{x}), \quad \boldsymbol{\zeta} \in S. \tag{12}$$

In the above form, Eq. 12 can only describe problems involving the motion of force-free cells in the fluid, the consequence of discarding the single-layer integral. We must complete the range by adding a velocity field generated by point forces and torques, leading to the velocity representation

$$u_{\mathrm{j}}(\mathbf{X}) - u_{\mathrm{j}}^{\infty} = -\sum_{\alpha=1}^{\mathrm{N}}\left(F_{\mathrm{i}}^{(\alpha)} - \frac{1}{2}(\mathbf{T}^{(\alpha)} \times \boldsymbol{\nabla})_{\mathrm{i}}\right)G_{\mathrm{ji}}(\mathbf{X}, \mathbf{x}_{\mathrm{c}}^{(\alpha)}) + \int_{\mathrm{S}} K_{\mathrm{ij}}(\mathbf{x}, \mathbf{X})\phi_{\mathrm{i}}(\mathbf{x})\, \mathrm{d}S(\mathbf{x}), \tag{13}$$

where $\mathbf{u}^{\infty}$ is the ambient fluid velocity (e.g., simple shear flow), $\mathbf{F}^{(\alpha)}$ and $\mathbf{T}^{(\alpha)}$ are the force and torque acting on cell $\alpha$, and $\mathbf{G}(\mathbf{X}, \mathbf{x}_{\mathrm{c}}^{(\alpha)})$ is the singularity solution corresponding to a point force placed at cell center $\mathbf{x}_{\mathrm{c}}^{(\alpha)}$. In all equations of this section, the subscripts represent spatial directors and the superscripts distinguish separate cells. Note that $\mathbf{u}^{\infty}$ can be any solution to the Stokes equation that vanishes at the wall. Evaluating Eq. 13 at the surface of cell $\beta$ produces the boundary integral equation

$$U_{\mathrm{j}}^{(\beta)} + (\boldsymbol{\omega}^{(\beta)} \times (\boldsymbol{\zeta} - \mathbf{x}_{\mathrm{c}}^{(\beta)}))_{\mathrm{j}} - u_{\mathrm{j}}^{\infty} = -\sum_{\alpha=1}^{\mathrm{N}}\left(F_{\mathrm{i}}^{(\alpha)} - \frac{1}{2}(\mathbf{T}^{(\alpha)} \times \boldsymbol{\nabla})_{\mathrm{i}}\right)G_{\mathrm{ji}}(\boldsymbol{\zeta}, \mathbf{x}_{\mathrm{c}}^{(\alpha)}) + \phi_{\mathrm{j}}(\boldsymbol{\zeta}) + (\mathcal{K}\phi)_{\mathrm{j}}(\boldsymbol{\zeta}), \quad \boldsymbol{\zeta} \in S_{\beta}, \tag{14}$$

where $\mathcal{K}$ denotes the double-layer integral operator, and $\mathbf{U}^{(\beta)}$ and $\boldsymbol{\omega}^{(\beta)}$ are the translational and rotational velocities of cell $\beta$, respectively.

The null space of $1 + \mathcal{K}$ is nontrivial and of dimension $6N$, so $6N$ additional linearly independent equations must be imposed to obtain a unique solution. This is accomplished by associating the force and torque on cell $\alpha$ with the null solutions on its surface:

$$F_{\mathrm{i}}^{(\alpha)} = \langle \phi^{(\beta,\mathrm{i})}, \phi \rangle, \tag{15}$$

$$T_{\mathrm{i}}^{(\alpha)} = \langle \phi^{(\beta,\mathrm{i}+3)}, \phi \rangle, \tag{16}$$

where $\phi^{(\beta,\mathrm{i})}$ corresponds to the translational ($i = 1, 2, 3$) and rotational ($i = 4, 5, 6$) motions of cell $\beta$, and the angled brackets denote the inner product

$$\langle \mathbf{f}, \mathbf{g} \rangle = \int_{\mathrm{S}} \mathbf{f}(\mathbf{x}) \cdot \mathbf{g}(\mathbf{x})\, \mathrm{d}S(\mathbf{x}). \tag{17}$$

The null solutions are appropriately normalized, such that $\langle \phi^{(\mathrm{n,i})}, \phi^{(\mathrm{m,j})} \rangle = \delta_{\mathrm{mn}}\delta_{\mathrm{ij}}$. The following boundary integral equation is solved for $\phi$:

$$\phi_{\mathrm{j}}(\boldsymbol{\zeta}) + (\mathcal{K}\phi)_{\mathrm{j}}(\boldsymbol{\zeta}) + \phi_{\mathrm{j}}^{(\beta,\mathrm{l})}(\boldsymbol{\zeta})\langle \phi^{(\beta,\mathrm{l})}, \phi \rangle = -u_{\mathrm{j}}^{\infty} + \sum_{\alpha=1}^{\mathrm{N}}\left(F_{\mathrm{i}}^{(\alpha)} - \frac{1}{2}(\mathbf{T}^{(\alpha)} \times \boldsymbol{\nabla})_{\mathrm{i}}\right)G_{\mathrm{ji}}(\boldsymbol{\zeta}, \mathbf{x}_{\mathrm{c}}^{(\alpha)}), \quad \boldsymbol{\zeta} \in S. \tag{18}$$

Once the double layer distribution $\phi$ is obtained, the surface velocity field can be calculated from Eq. 13 as

$$u_{\mathrm{j}}(\boldsymbol{\zeta}) = -\phi_{\mathrm{j}}^{(\beta,\mathrm{l})}(\boldsymbol{\zeta})\langle \phi^{(\beta,\mathrm{l})}, \phi \rangle, \quad \boldsymbol{\zeta} \in S. \tag{19}$$

The rigid body motions of cell $\alpha$ can then be extracted from Eq. 19 by taking the inner product of Eq. 19 with $\phi^{(\alpha,\mathrm{m})}$ and using the orthonormal property of the null functions.

The integral operator in Eq. 18 is simply the integral operator in Eq. 13 plus a sum of the first-rank operators $\phi^{(\beta,\mathrm{l})}\langle \phi^{(\beta,\mathrm{l})}, \cdot \rangle$ involving the null solution of $1 + \mathcal{K}$. This shifts the $-1$ eigenvalue of the double-layer operator to zero, a technique known as Wielandt's deflation. An eigenvalue at $+1$ still prevents iterative solution of Eq. 18. A second deflation makes use of the eigenvectors of the adjoint operator $\mathcal{K}^{\dagger}$:

$$\psi^{(\beta)}(\boldsymbol{\zeta}) = \begin{cases} \hat{\mathbf{n}}/\sqrt{S_{\beta}}, & \boldsymbol{\zeta} \in S_{\beta}, \\ 0, & \boldsymbol{\zeta} \in S_{\beta}. \end{cases} \tag{20}$$

These eigenvectors are simply the unit normals on the $N$ cells. The sum of the first-rank operators $\psi^{(\beta)}\langle \psi^{(\beta)}, \cdot \rangle$ are subtracted from the operator in Eq. 18, producing the final form of the CDL-BIEM equation,

$$\phi_{\mathrm{j}}(\boldsymbol{\zeta}) + (\mathcal{K}\phi)_{\mathrm{j}}(\boldsymbol{\zeta}) + \phi_{\mathrm{j}}^{(\beta,\mathrm{l})}(\boldsymbol{\zeta})\langle \phi^{(\beta,\mathrm{l})}, \phi \rangle - \psi_{\mathrm{j}}^{(\beta)}(\boldsymbol{\zeta})\langle \psi^{(\beta)}, \phi \rangle = b_{\mathrm{j}}(\boldsymbol{\zeta}) - \tfrac{1}{2}\psi_{\mathrm{j}}^{(\beta)}\langle \psi^{(\beta)}, \mathbf{b} \rangle, \quad \boldsymbol{\zeta} \in S, \tag{21}$$

where

$$b_{\mathrm{j}}(\boldsymbol{\zeta}) = -u_{\mathrm{j}}^{\infty} + \sum_{\alpha=1}^{\mathrm{N}}\left(F_{\mathrm{i}}^{(\alpha)} - \frac{1}{2}(\mathbf{T}^{(\alpha)} \times \boldsymbol{\nabla})_{\mathrm{i}}\right)G_{\mathrm{ji}}(\boldsymbol{\zeta}, \mathbf{x}_{\mathrm{c}}^{(\alpha)}), \quad \boldsymbol{\zeta} \in S. \tag{22}$$

Eq. 21 can be solved by successive iteration for $\phi$. The rigid body motions of the cells then follow directly from Eq. 13.

As the surface-to-surface separation ($\epsilon$) between cells becomes small, the fluid exerts strong lubrication forces on the cells that increases singularly as either $1/\epsilon$ or $\log(1/\epsilon)$. To fully capture these lubrication forces, it is necessary to refine the mesh over areas in proximity to another surface, so that the local surface shape is resolved. This increase in the number of boundary elements puts additional demands on computational time (time ~ $N_{\mathrm{el}}^{2}$) that, for the purposes of the present study, are unsatisfactory. To reconcile this, a coarse discretization of 24 elements per sphere is used, which fails to capture the lubrication forces when the cells come near contact with each other or with the planar surface. The neglected lubrication forces can then be added in as external forces from known analytic solutions. The expressions for the cell–cell and cell–surface lubrication forces are given in the Appendix. The main feature of those forces is that shearing motion of two close surfaces produces leading-order terms of order $\log(1/\epsilon)$ and $\epsilon \log(1/\epsilon)$, whereas the squeezing motion of two approaching spheres is a stronger singularity with an additional term of order $1/\epsilon$. The lubrication solution is matched with the outer numerical solution at $\sim 0.1a$ for shearing motion and $0.2a$ for squeezing motion. The various lubrication forces depend on the relative velocity between surfaces, and an average of past values is used in the multiparticle adhesive dynamics (MAD) simulation. This does not pose a problem because, in general, the cell velocities are continuous and slowly varying functions. The exception is directly after bond breakage, a rare event, when a sharp jump in the overall force balance creates a discontinuity in the cell motions. At this point in the simulation, the correct velocity is obtained by iteration.

After the cells' rigid body motions are obtained from the CDL-BIEM calculation, they are fed into the AD portion of the simulation. The cells, and all of the adhesion molecules on their surfaces, are translated and rotated in space according to the cell velocities. The existing bonds are checked for

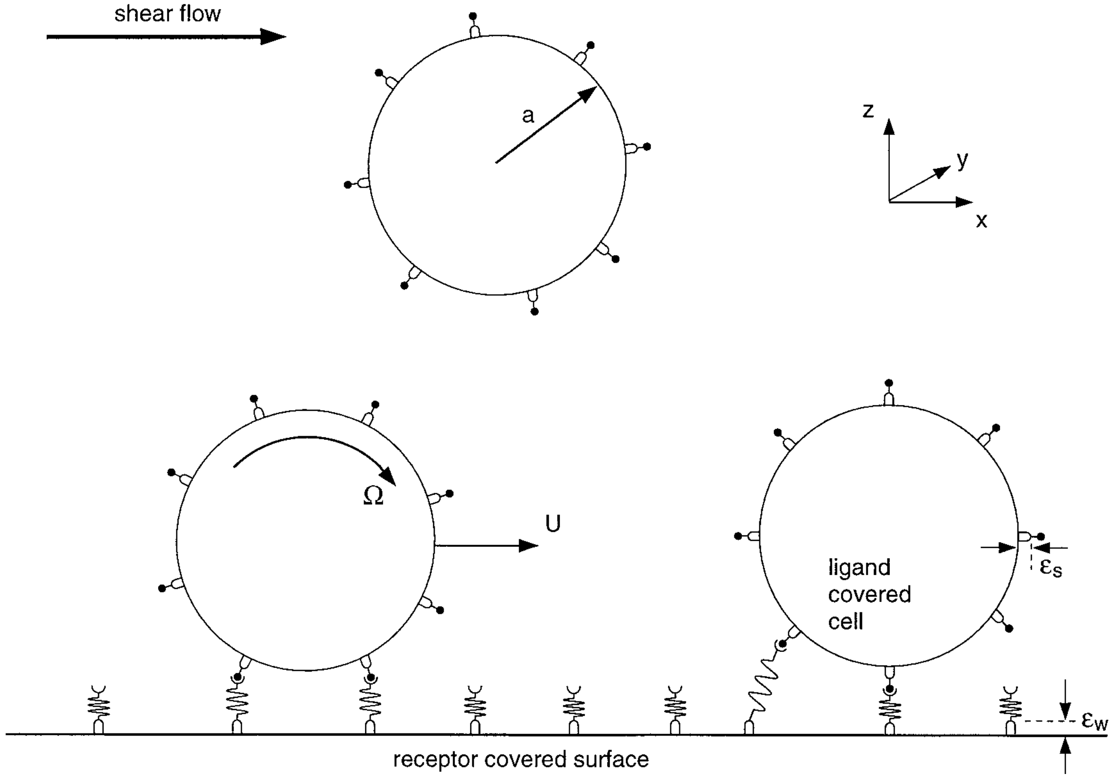

FIGURE 1 Schematic diagram of MAD. Far from the cells, the external flow is a linear shear flow, but the motion of the cells is coupled through a complex disturbance flow. A layer of surface roughness elements is placed outside of the hydrodynamic radius $a$ to account for the fact that cells (or beads) are not mathematically smooth spheres. The plane has its own roughness, of length $\epsilon_w$.

breakage using updated values for the bond length as required by Eq. 2. Next, all of the unbound molecules in the contact area are checked for formation (an increasingly likely event in the case that the cell has moved closer to the surface over the previous time step). The external forces and torques are then summed up over each cell. At this stage in the simulation, we are again ready to perform the mobility calculation. Thus, the multiparticle mobility calculation is fused with AD in a sequential manner.

## Numerical implementation

The surface of each sphere is discretized into 24 QUAD9 elements—quadralateral elements with three nodes per edge and one center node. The elements are arranged by dividing each side of a cube into four square elements and then projecting this (inscribed) cube onto the surface of a sphere. The elements are interpolated with second-order Lagrangian polynomials, and integrals evaluated with an adaptive Gaussian quadrature. A $1 \times 1$ quadrature is sufficiently accurate for double integrals over distant elements, whereas $2 \times 2$ quadrature is used for nearby elements and elements close to the wall. Rotating the meshes so that the "spines" on nearby cells face each other achieves velocities accurate to within 3%. The iteration in Eq. 21 coverges quite rapidly, generally requiring only one iteration from the previously obtained value for $\boldsymbol{\phi}$ to achieve a relative error of $O(10^{-4})$. The large separation of length scales between the deviation bond length and the cell radius ($|\mathbf{x}_b - \lambda|/a \sim 10^{-3}$) requires that very small time steps be used, $dt = 10^{-7}$ s in most cases. Fortunately, the mobility calculation, whose double integrals are by far the most demanding computational task in the simulation, does not need to be performed at each time step. In practice, the AD Monte Carlo simulation is performed at each step, with the cell mobilities updated when the external forces have changed by a significant amount ($\Delta F/F \sim 10^{-3}$).

## Experimental

The exact experimental protocol of Rodgers et al. (2000) was followed to prepare surfaces to be used in the in vitro experiments of selectin-mediated rolling; details of the chemistry and preparation of materials is precisely as described therein. Streptavidin-coated microspheres of radius 5.4 $\mu$m were covered with sialyl Lewis$^x$ (sLe$^x$) through a sLe$^x$-PAA-biotin linkage. Sialyl Lewis$^x$ is the functional carbohydrate domain presented by many selectin-binding ligands such as P-selectin glycoprotein-1 (PSGL-1). The beads were then suspended in a phosphate-buffered saline (PBS)/1% bovine serum albumin (BSA) solution. Polystyrene slides were incubated with soluble P-selectin and later washed with PBS and 2% BSA to block nonspecific adhesion. The substrate is then placed in the well of a parallel plate flow chamber. Flow is driven by a syringe pump, and the system is imaged from below using an inverted-phase contrast microscope equipped with a high-speed video recorder. Surface coverages were 90 molec/$\mu$m$^2$ of sLe$^x$ on the bead surface and 180 molec/$\mu$m$^2$ of P-selectin on the substrate, densities that support slow rolling motion over shear rates of 80–160 s$^{-1}$. A dilute suspension of carbohydrate-coated beads in buffer solution, 0.03% by volume, was perfused over the selectin-presenting surface. Many of the beads sediment to the surface and adhesively roll across the field of view. Experiments were recorded on video tape for later analysis.

To achieve area fractions of up to 10% bound cells, for the study of the effect of area fraction on rolling velocity, a different procedure was necessary. A relatively concentrated sample of 3 million beads in 50 $\mu$L of buffer was prepared (3% by volume). For each experimental trial, 5 $\mu$L were injected into the flow chamber using a microsyringe inserted into a septum at the flow chamber entrance. The beads were then

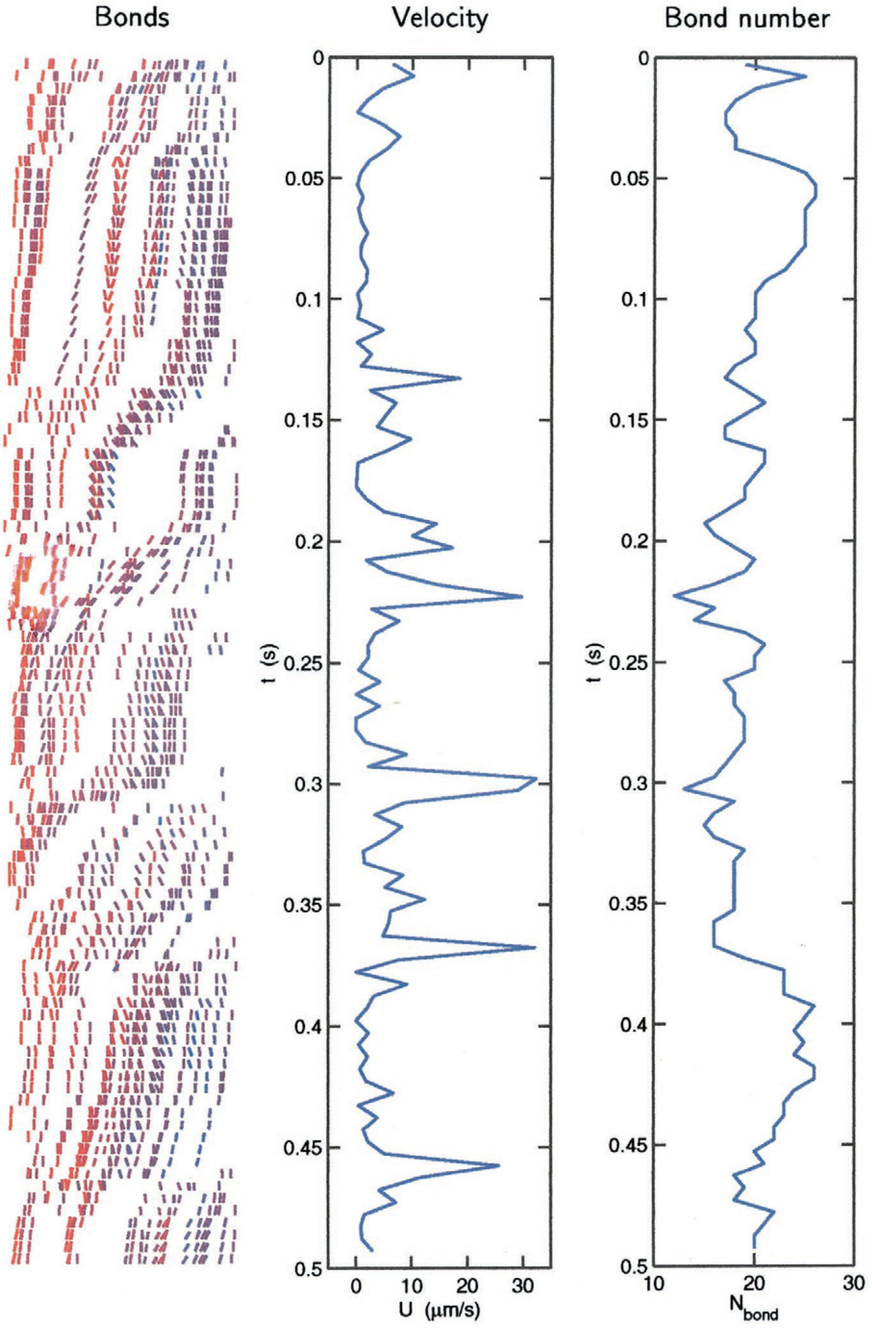

FIGURE 2 Simulation of an isolated cell rolling over P-selectin at $\dot{\gamma} = 100$ $s^{-1}$ (value of $k_f^0 = 500$ $s^{-1}$ used). The columns represent: (*left*) Color-coded snapshots of the bonds in the contact area. Extended bonds appear red, whereas compressed bonds appear blue. The cell is moving from left to right as time increases. Times correspond to the scale shown on the two other sets of axes, increasing from top to bottom. (*center*) Translational velocity of the spherical cell. (*right*) The instantaneous number of bonds between the cell and planar boundary.

allowed to settle for approximately 1 min before flow was initiated. This technique resulted in a high concentration of adhesively rolling beads on the surface.

## RESULTS

### Single cell rolling

Figure 2 shows results from a simulation of isolated cell rolling. As in the original AD simulation, these isolated cell results were generated by solving the analytic 6 × 6 mobility matrix (Eq. 7). The parameter values used in the current study are given in Table 1. Plotted in the leftmost column of Fig. 2 are snapshots of the bonds in the contact area at various times during the simulation, viewed from the side (shear flow is from left to right). Choosing a frame of reference moving with the cell gives the bonds the appearance of being convected through the contact area toward the left. The bonds are colored so that extended bonds are shown in red, whereas those bonds existing in a compressed state are shown in blue. Note the distribution of extended versus compressed bonds—stretched bonds are almost exclusively found at the trailing edge of the contact area, whereas bonds at the front of the contact area are often

**TABLE 1 Values of physical parameters used in simulations**

| Parameter | Definition | Value |
|---|---|---|
| $a$ | particle radius | 5 $\mu$m |
| $\dot{\gamma}$ | shear rate | 80–160 $s^{-1}$ |
| $\mu$ | viscosity | 0.01 P |
| $\rho$ | fluid density | 1.0 g/cm$^3$ |
| $\Delta\rho$ | density difference | 0.05 g/cm$^3$ |
| $\epsilon_s$ | sphere roughness | 175 nm |
| $\epsilon_w$ | wall roughness | 50 nm |
| $\sigma$ | spring constant | 100 dyn/cm |
| $\lambda$ | equilibrium bond length | 30 nm |
| $k_r^0$ | unstressed off-rate | 2.4 $s^{-1}$ |
| $r_0$ | reactive compliance | 0.39 Å |
| $k_f^0$ | intrinsic on-rate | 365 $s^{-1}$ |
| $T$ | temperature | 298 K |
| $n_r$ | receptor density | 90–150 molec/$\mu$m$^2$ |

Bell model parameters for P-selectin/PSGL-1 are taken from Smith et al. (1999).

compressed after formation. The clustering of bonds that arises from the stochastic nature of binding and unbinding, and random distribution of adhesion molecules, can be readily seen in Fig. 2. The center column shows how the translational velocity of the bound cell correlates with the instantaneous bond state. Note that the breakage of a cluster of bonds at the trailing edge at times $t = 0.13, 0.19, 0.29$ s results in a brief jump in the rolling velocity, and the breakage of a cluster of bonds directly beneath the cell at $t = 0.45$ s causes a similar jump. As can be seen in the rightmost column, these increases in the translational velocity cause multiple bond formation events. This effect, pointed out by Chang and Hammer (1999), is due to the increase in molecular encounter rate as the two surfaces slip past each other.

## Multiparticle algorithm efficiency

As a demonstration of the equivalence of the current multiparticle mobility calculation with other methods, Table 2 presents CDL-BIEM results with added lubrication forces (no adhesion) along with results obtained via Stokesian dynamics by Bossis et al. (1991). The problem studied is that of one or two spheres in the vicinity of a plane translating parallel to the plane because of an imposed force directed parallel to the axis of symmetry. The friction coefficient $\xi_x$ is defined as $F_x = \xi_x \times U_x$, and nondimensionalized by $6\pi\mu a$. The level of agreement exhibited in Table 2, achieved economically by using only 24 elements per sphere, is sufficient for the purposes of the present study. The extent to which $2 \times (\xi_x)^{N=1} - (\xi_x)^{N=2} > 0$ indicates the level of screening from the external fluid motion that the spheres experience. Under an imposed shear flow, this screening causes a lowered translational velocity for closely spaced spheres aligned with the flow. Figure 3 shows the translational velocity of a pair of force-free (nonadhesive) spheres located $0.01a$ above a plane under simple shear. The velocity in the $x$-direction, scaled by $\dot{\gamma}a$, is equal for both spheres, with the transverse velocities equal to zero for all separations. The uneven grid spacing for this calculation was chosen based on the expectation of a $1/r^2$ attenuation with distance of the interaction between force-free rigid spheres in Stokes flow. Note that the velocity monotonically increases as $\Delta x$ or $\Delta y$ increases, and that the screening effect persists roughly twice as far in the streamwise direction as in the transverse direction. Only one quadrant needs to be plotted, due to the two-fold symmetry across the $\Delta x$, $\Delta y =$ 0 planes.

**TABLE 2 Comparison of CDL-BIEM mobility calculation with Stokesian Dynamics results of Bossis et al. (1991)**

| h | $(\xi_x)^{N=1}$ | $(\xi_x)^{N=2}$ |
|---|---|---|
| Present study | | |
| 50.0 | 1.01 | 1.31 |
| 2.0 | 1.38 | 1.90 |
| 1.01 | 3.41 | 5.73 |
| $1.0 + 10^{-6}$ | 8.31 | 15.56 |
| Stokesian Dynamics | | |
| 50.0 | 1.0 | 1.3 |
| 2.0 | 1.4 | 1.9 |
| 1.01 | 3.4 | 5.6 |
| $1.0 + 10^{-6}$ | 8.3 | 15.4 |

## Pairs of rolling cells

### Experiments

Pairs of sLe$^x$-coated beads were experimentally observed rolling near each other on P-selectin surfaces to determine the effect of spatial separation on average rolling velocity. A pair was selected for measurement when it was at least 20 radii away from any other bound bead to isolate binary interactions for study. Figure 4 shows a plot of the average rolling velocity as a function of the center-to-center separation in the streamwise ($x$) and transverse ($y$) directions at a shear rate of $\dot{\gamma} = 80\ s^{-1}$. Figure 4 was generated from 209 observed pairs ($\Delta t \approx 3$ s), by averaging all data points within a 4-$\mu$m-radius circle at each location. Symmetry in $x$ and $y$ was assumed in constructing the figure. Grid locations that contained less than five points were excluded from Fig. 4. The general trend is that, as the separation distance between the two beads decreases, both beads slow down, consistent with the increasing cell–cell drag as illustrated in Fig. 3. As is the case for force-free (nonadhesive) spheres, the hydrodynamic interactions persist roughly twice as far in the streamwise ($x$) direction as in the $y$-direction. One feature in Fig. 4 that is absent when only hydrodynamic interactions are included between particles is the existence of two local minima in rolling velocity, centered at ($\Delta x$, $\Delta y$) = (9, 13) and (14, 4). A localized region of increased velocity was observed at ($\Delta x$, $\Delta y$) = (30, 11). Note that pairs of beads aligned with the flow ($\Delta y = 0$) and closer

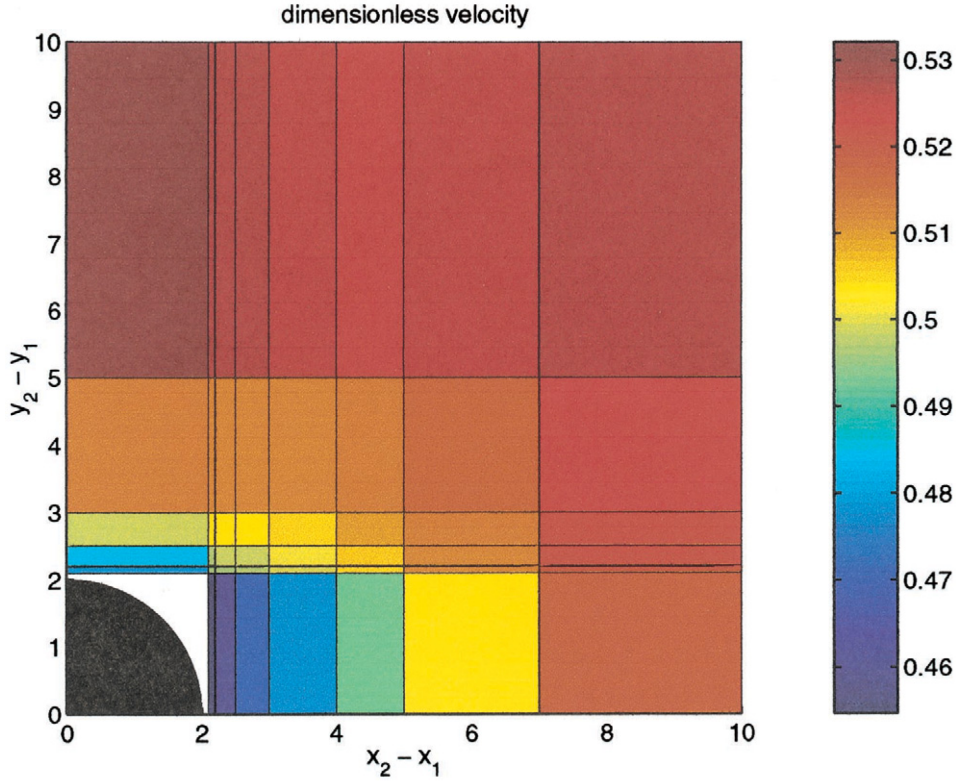

FIGURE 3 The dimensionless translational velocity of two spheres elevated 0.01 radii above a plane in shear flow, as a function of the relative center-to-center separation between spheres scaled with the radius. A grid spacing appropriate to interactions that decay as $1/r^2$ was used.

than 3 radii are generally not observed, implying that this is an unstable configuration.

To this point, we have not addressed the issue of stability of a rolling pair, i.e., the relative tendency of a pair of rolling cells to remain at their initial separation. Figure 5, generated from the experimental data of Fig. 4, shows the average deviation velocity between rolling pairs of beads. From this set of data representing 209 pairs, there appears to be a systematic variation of deviation velocity with respect to separation in the $x$- and $y$-directions. In particular, outer configurations around $\Delta x$, $\Delta y \sim 20$ $\mu$m are more unstable, whereas, at separations ($\Delta x$, $\Delta y$) = (12, 15) and (20, 7) $\mu$m, the deviation velocity approaches zero. Note that the separation (25, 0) appears to locally attract nearby configurations. This result suggests that trains of rolling cells aligned with the flow, and of sufficient separation, are stable hydrodynamically.

### *Simulations*

Simulations of pairs of rolling cells at different separations were performed for the conditions of Fig. 4, for direct comparison. In each simulation, pairs of spheres were given a steady-state bond configuration, and integrations to determine the effects of hydrodynamic interactions were carried out for a period of 0.2–0.25 s. Configurations of pairs of cells corresponding to $\Delta x$ = (0, 4, 9, 15, 20, 25, 30) and $\Delta y$ = (0, 3, 7, 10, 13, 17, 22) were simulated. The results are presented in Fig. 6, with calculations for separation distances different from the above values obtained by interpolation. Note the remarkable level of agreement with the spatial pattern of rolling velocities observed experimentally shown in Fig. 4. In particular, local minima of decreased velocity are evident at ($\Delta x$, $\Delta y$) = (8, 13) and (15, 3), as was observed experimentally. A very distinct region of faster rolling behavior is also seen at ($\Delta x$, $\Delta y$) = (27, 12) in direct agreement with experiment. The only significant difference found between theory and experiment is that the decrease in rolling velocity is more pronounced in the simulated system, perhaps due to the surrounding beads, or the heterogeneity in surface coverage that exists in the real system but is absent in the idealized model.

The instantaneous behavior of pairs of rolling cells reveals differences in the dynamics of rolling that are induced by the proximity of cells. Figure 7 shows representative traces of the instantaneous velocity for pairs of rolling particles, calculated for discrete intervals of $10^{-3}$ s and two different cell separations. Note that the cells in the configuration $\Delta x$ = 20 $\mu$m, $\Delta y$ = 0 experience longer pauses and spend more time in a stationary state, compared to the pair with separation $\Delta x$ = 15 $\mu$m, $\Delta y$ = 22. The spatial dependence of the pause time in rolling is quantified in Figs. 8 and

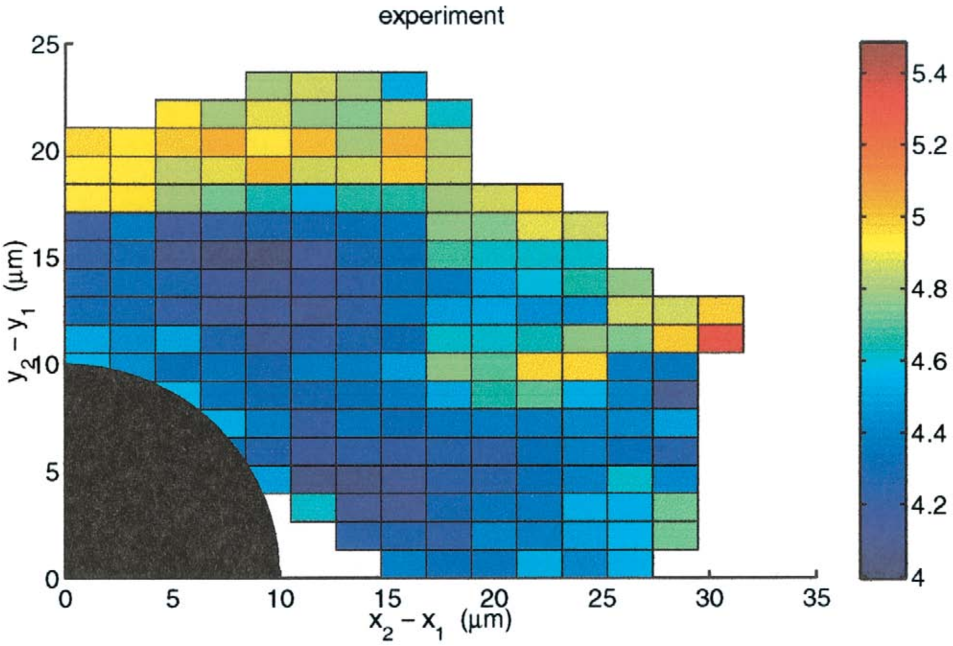

FIGURE 4 The experimental rolling velocity of pairs of adhesively bound beads in contact with a plane, as a function of separation between beads. The scale on the right shows velocities in μm/s.

9. Figure 8 is a plot of the average fraction of time that the rolling pair of cells pauses, defined as $U < 0.05$ μm/s. This critical value is roughly 1% of the average rolling velocity. Note that the spatial variation in the fraction of time paused follows a trend that is roughly the inverse of the average velocity of Figs. 4 and 6. Thus, in addition to rolling with a slower average velocity, cells that are nearby each other and aligned with the flow spend more of their time in a paused state. As can be seen from Fig. 9, these pauses tend to last longer for closely separated cells.

The simulation allows us to examine the behavior of a rolling pair of cells at a higher resolution than can be easily accessed by experiment. The separation distance between two rolling cells undergoes a random walk in the two dimensional $\Delta x$–$\Delta y$ space, as can be seen from the two trajectories in Fig. 10. From such trajectories, a random "pair" diffusivity can be numerically calculated from the mean-square displacement as

$$D_p = \langle \bar{x}^2 \rangle / 4t. \tag{23}$$

The square root of the pair diffusivity is plotted in Fig. 11 as a function of separation distance. Note that this quantity behaves similarly to the average velocity of Figs. 4 and 6. The largest fluctuations in motion are found at the farthest separations, and, as the cells approach each other, the diffusivity decreases. Taken with the experimental result of Fig. 5, showing the time- and particle-averaged relative motion of a pair of beads, one may conclude that pairs of rolling leukocytes will roll with a separation that does not change (become more stable) with respect to each other when they become closer and aligned with the flow.

## Ensembles of rolling cells

### Experiments

Experiments were performed at a higher concentration of adherent beads than previously described in this paper to explore the influence of ensembles of cells on average rolling velocity. The symbols in Fig. 12 show the experimentally measured average rolling velocity as a function of area fraction of bound beads on the surface. The area fraction includes a minority of stationary beads that are unavoidably present on the surface. This is a justified approximation, because their velocity is much closer to that of rolling cells than freestream beads or fluid. Each experimental point was obtained by averaging over 3–5 seconds and between 37 and 83 beads, with the error bars representing the uncertainty in the mean value propogated from the random variation among rolling beads. Despite considerable scatter in the data, the trend is clearly that increasing the area fraction of bound beads decreases the average rolling velocity.

### Simulations

The experimental data are compared to results obtained from simulations of an $N = 14$ hexagonal array of model cells (see Fig. 13). Each cell was given a steady-state bond

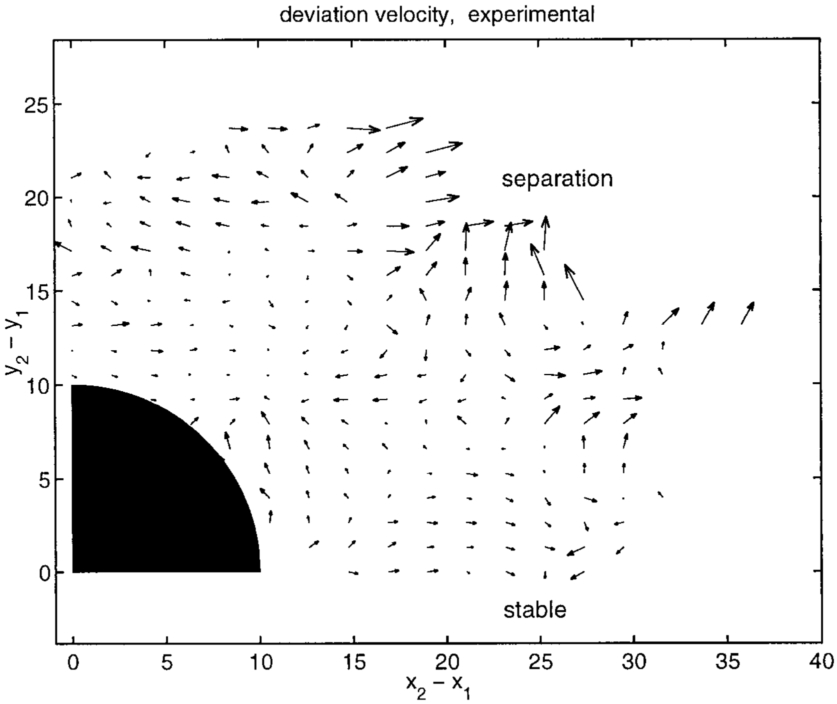

FIGURE 5 Vector field of the deviation motion between pairs of rolling beads, obtained from experiment. Note that $\Delta x$, $\Delta y \sim 20\ \mu$m is an unstable configuration, whereas other configurations such as $\Delta x = 25\ \mu$m, $\Delta y = 0$ are more stable.

configuration and each simulation carried out for ~0.03 s, requiring ~140 hours of computational time per run on an SGI Octane 300 MHz workstation. The level of agreement between simulation and experiment in Fig. 12 is quite good, particularly considering that the experimental beads are often configured randomly on the surface. It is interesting to note that, if the average velocity is plotted versus the square root of area fraction, the two curves are linear in appearance

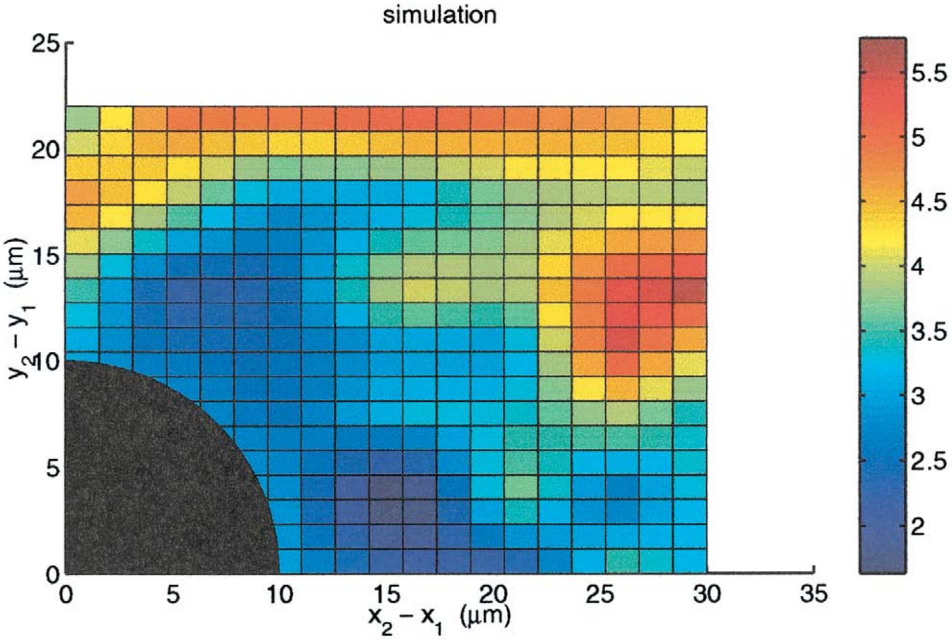

FIGURE 6 The simulated rolling velocity of pairs of adhesively bound cells in contact with a plane, as a function of separation between cells. The scale on the right shows velocities in $\mu$m/s.

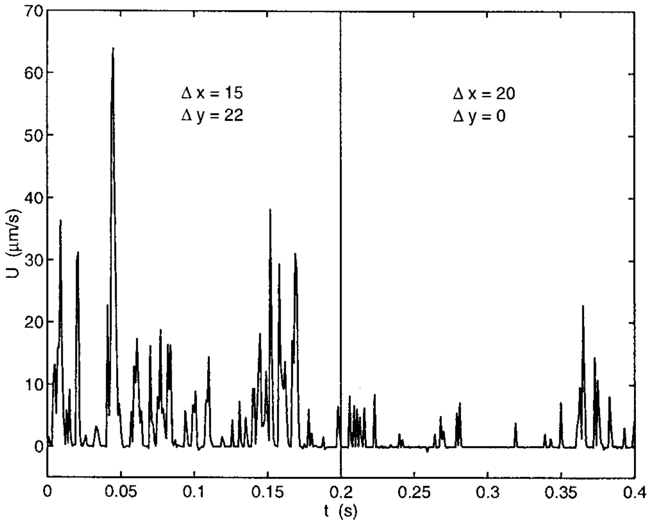

FIGURE 7 The instantaneous velocity at two different cell separations, obtained from binary simulations.

(not shown). This is indicative of the $1/r$ dependence of the Stokeslet induced by a sphere under external force. An elevated value of $n_{\mathrm{site}}$ was used at the higher shear rate, as discussed below.

From a simple consideration of the scaling of the cell rolling problem, one would expect that the dimensional rolling velocity should scale as the square of the shear rate, because both the imposed shear force and the ambient flow are first-order in this quantity. However, considerable evidence collected from cell-free experiments (Brunk and Hammer, 1997; Rodgers et al., 2000; Greenberg et al., 2000) show that the dependence of rolling velocity on shear rate is, at most, first-order over a range of parameter values and receptor species. Although the weak dependence of rolling velocity on shear rate observed for leukocytes at high shear (e.g., Goetz et al., 1994) is most likely due to a flattening of the cell and enlargement of the contact area, that mechanism is eliminated in a system featuring rigid beads. Chang and Hammer (2000) addressed this effect in terms of the heterogeneity in the site densities of sLe$^{\mathrm{X}}$ on prepared samples of beads. Beads prepared using the protocol of Brunk et al. (1996) have been shown to possess a normal distribution of carbohydrate surface coverages, with a standard deviation roughly equal to the mean value. The implication is that, although, at lower shear rates, the majority of the bead population supports stable rolling, when the shear rate is increased, the lower tail of the distribution is swept off of the surface. Thus, at higher shear rates, the observer is measuring the averaged behavior of a subpopulation of beads that possess a higher mean site density of sLe$^{\mathrm{X}}$. This is consistent with our qualitative observations that fewer beads roll at the higher shear rate. Chang and Hammer (2000) demonstrate that AD simulations of heterogeneous distributions of cells are able to reproduce the approximately linear dependence of rolling velocity on shear rate quite accurately over a wide range of parameter values. Due to demands on computational time, for the present study, we have performed simulations of homogeneous collections of cells possessing an elevated mean site density. Treated as an adjustable parameter to match the experimental data, a value of $n_{\mathrm{site}} = 150$ molec/$\mu$m$^2$ was

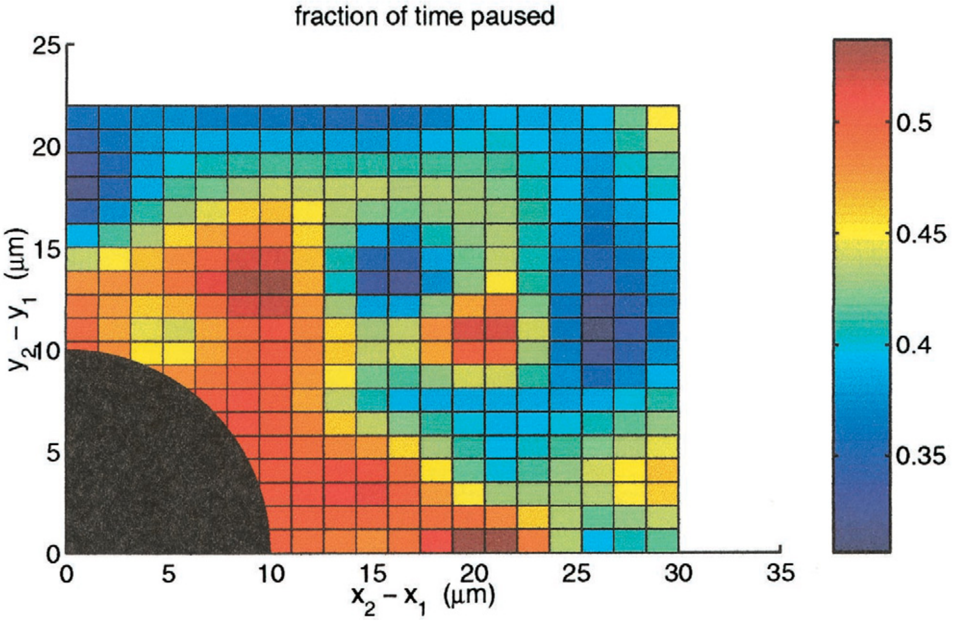

FIGURE 8 The fraction of time that a simulated pair of rolling cells have an instantaneous velocity $U < 0.05$ $\mu$m/s, as a function of separation between cells.

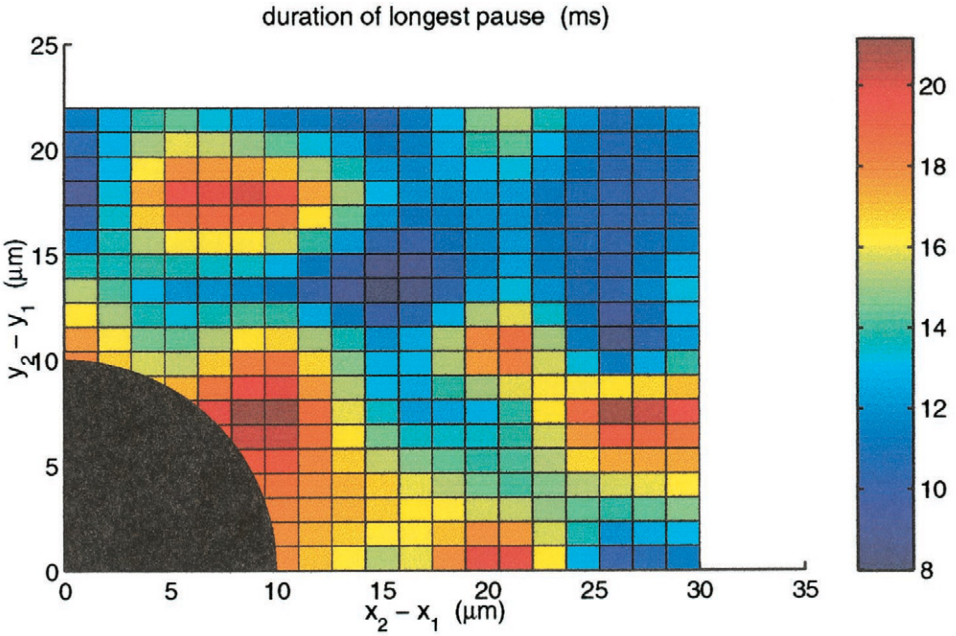

FIGURE 9 The duration of the longest pause (defined as $U < 0.05$ μm/s) during simulations of length 0.2–0.25 s, as a function of separation between cells. Results are presented in units of milliseconds.

chosen at $\dot{\gamma} = 160\ \text{s}^{-1}$, increased from the measured mean density of $n_{\text{site}} = 80\ \text{molec}/\mu\text{m}^2$ (used for the simulations at $\dot{\gamma} = 80\ \text{s}^{-1}$). If the lower site density is used in simulations at $\dot{\gamma} = 160\ \text{s}^{-1}$, rolling velocities of $U \approx 35$ μm/s are predicted, far greater than what is observed experimentally.

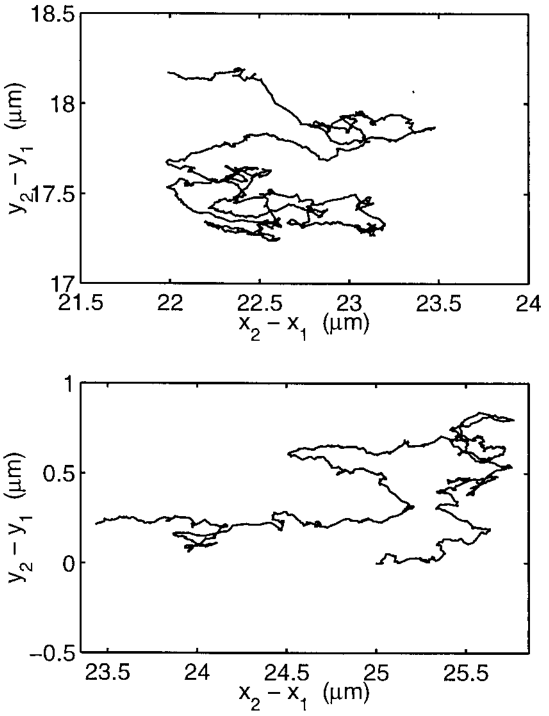

FIGURE 10 The separation between rolling cells undergoes a random walk in two dimensions. Data obtained from simulations at $\dot{\gamma} = 80\ \text{s}^{-1}$, $t_f = 1$ s, and initial separations of $(\Delta x_0, \Delta y_0) = (22.5, 17.5)$ and $(25, 0)$ μm.

## DISCUSSION

We have presented a simulation method capable of simulating the behavior of adhesive spheres reversibly interacting with an adhesive surface under flow. This represents an extension of the AD algorithm of Hammer and Apte (1992), to include hydrodynamic and chemical interactions between multiple cells in suspension. The MAD simulation is ideally suited to studying the adhesive interactions of blood cells with the bounding surfaces of venules, and can also be applied to the study of colloidal particle aggregation in the presence or absence of flow. As an example of the utility of the current methodology, we have applied it to the case of spherical model leukocytes rolling on P-selectin in a parallel-plate flow chamber. Good agreement was found between the theory and cell-free experiments, with both demonstrating that rolling cells slow each other down as they approach contact. The deviation motion between rolling cells was found to decrease as the cells approach each other or when they align with the flow. Taking these findings into account, we can comment on recent experiments of Kunkel et al. (1998), where clusters of rolling leukocytes were observed in stimulated mouse cremaster muscles.

Kunkel et al. (1998) studied the accumulation of leukocytes in mouse cremaster muscles after inflammation is induced by treatment with tumor necrosis factor-$\alpha$. They observed the formation of dynamically stable clusters of about 10 cells, with

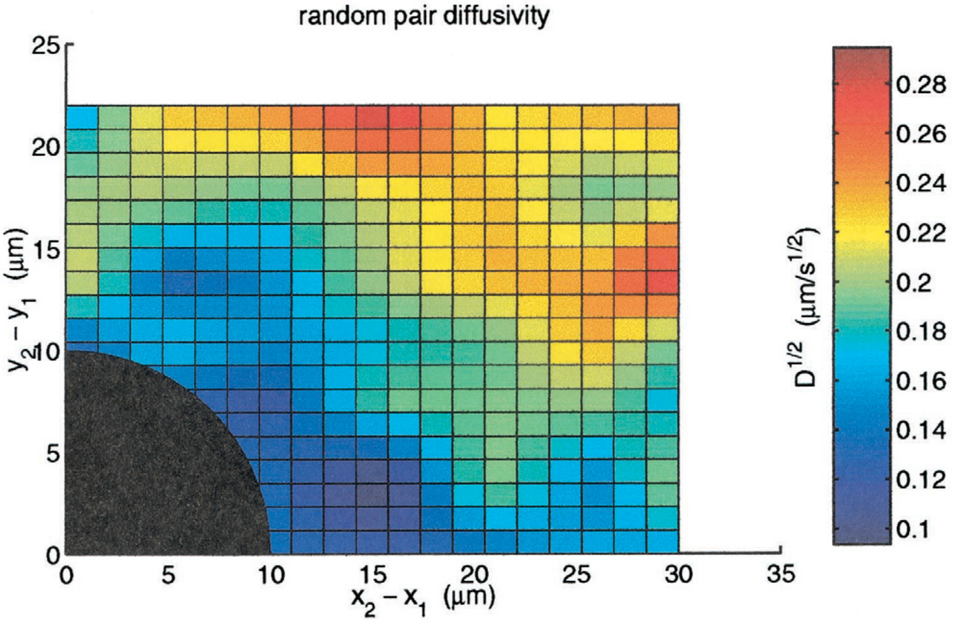

FIGURE 11 The square root of the random diffusivity between pairs of rolling cells, as a function of initial separation. Note that this quantity exhibits a spatial dependence similar to the average velocity given in Figs. 4 and 6.

an average cluster length of 32 μm and cluster width of 27 μm. They analyzed 476 leukocytes to determine the mechanism by which cells are recruited into clusters, with possible cell–cell-mediated or endothelial-mediated mechanisms hypothesized. Kunkel et al. show that the cell clusters, as defined by measuring the local concentration of rolling cells, are approximately stationary with respect to the streamwise coordinate; the authors conclude that the cluster formation is due to locally elevated levels of E-selectin expression. Such indirect determination of molecular concentration is necessary because current experimental methods are capable of measuring selectin expression at the organ level, but not in segments of individual microvessels.

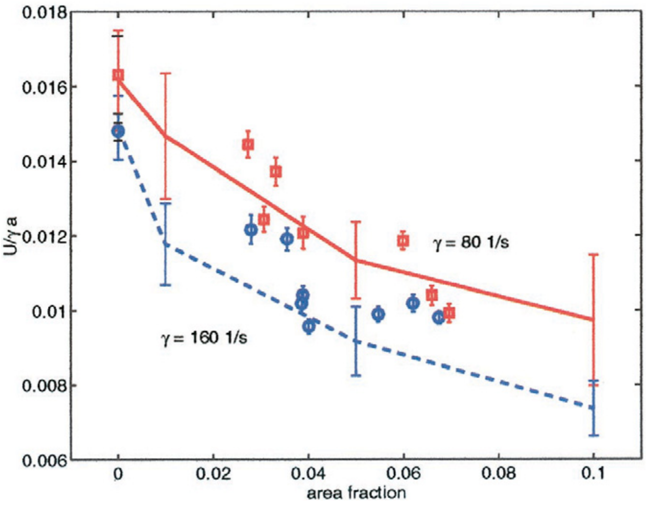

FIGURE 12 Rolling velocity, scaled by $\dot{\gamma}a$, as a function of the area fraction of bound spheres on the surface. The symbols represent averaged experimental observations, and the lines represent simulations of hexagonal arrays of 14 cells. The squares and solid lines denote the lower shear rate, and circles and broken lines denote the higher shear rate.

The current study can lend insight into the work of Kunkel et al. and affords a different possible interpretation of their results. At steady state, a cluster of slowly rolling cells maintains its size by adding cells at the upstream edge that catch up to the cluster, and, by losing cells at the downstream edge that experience a lower cell concentration than cells in the cluster's interior. Due to the symmetry of binary interactions (Figs. 3, 4, and 6), it requires at least three rows of cells for a steady-state cluster to exist. In a three-row cluster, the interior row experiences roughly twice the level of sheltering from the shear flow as compared to cells at the leading and trailing edges of the cluster.

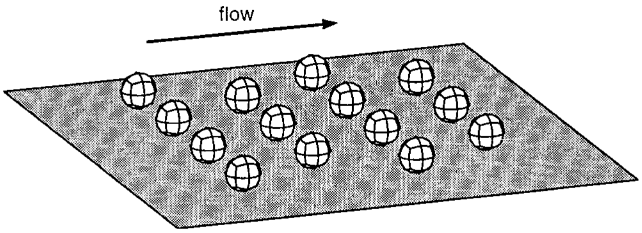

FIGURE 13 The array of 14 cells used in the simulations of Fig. 12. This spacing corresponds to an area fraction of 10% in a box defined by the cell centers. Note the 24-element QUAD9 surface discretization used in the current study.

Thus, the upstream flux produced by cells leaving the downstream edge of the cluster and cells joining the upstream edge of the cluster provides a mechanism for a nearly stationary concentration wave of rolling cells. It is perhaps to be expected, then, that an array of 3 × 3 closely spaced cells is close to the average cluster size of 10 found by Kunkel et al. Their average cluster is slightly longer than it is wide, in direct agreement with the level of spatial attenuation found for binary interactions in this study. As a final note on the experiments of Kunkel et al., their classification scheme of a one-diameter separation or less to qualify as cell–cell-induced recruitment is too stringent, and probably underestimates the importance of cell–cell interactions. This is pointed out in light of the present results, which show that significant interactions persist at center-to-center separations in excess of six radii.

It is important to consider the implications of cell–cell interactions for the dynamics of biological processes such as inflammation. It is well established that neutrophil rolling is noisy, with substantial fluctuations in rolling velocity and periods of pausing. These dynamics are displayed for neutrophils rolling on endothelium (Goetz et al., 1994), for neutrophils rolling in blood vessels (Lipowsky et al., 1991), and sLe$^x$-coated beads rolling on selectins (Brunk and Hammer, 1997; Rodgers et al., 2000; present study). There is a rough correlation between rolling velocity and the pause-time distribution (Chang, 1996); Figs. 8 and 9 of this paper demonstrate that this correlation can be modulated by cell–cell hydrodynamic interactions. In inflammation, neutrophil diapedesis requires firm adhesion through $\beta_2$ integrins, which follows and requires selectin-mediated rolling in some complex way. Simon and coworkers recently showed that neutrophil rolling on E-selectin can directly lead to activation of $\beta_2$ integrins (Simon et al., 2000). Also, E- and P-selectin double knockout mice display no inflammation (Bullard et al., 1996), suggesting that selectin-mediated rolling is required for firm adhesion. We have speculated that the precise dynamics of rolling is important for the transition to firm adhesion in two potential ways. First, if signals are generated by selectin occupancy, the precise dynamics of rolling affects selectin occupancy and therefore activation. Second, it is much more likely for $\beta_2$ integrins to bond during slow rolling or substantial pausing; thus, noisy, slower motions likely facilitate the transition to firm adhesion. Therefore, the effects demonstrated and calculated here—that cell–cell hydrodynamic interactions can influence the dynamics of cell rolling—can have important implications for the regulation of the transition to firm adhesion. Like the shear threshold effect (Finger et al., 1996), this paper explains a means by which hydrodynamic interactions can affect dynamics of cellular adhesion phenomena, with possibly important implications for physiology.

To bring the current research closer to a complete simulation of blood flow, details such as viscoelastic microvilli with receptors localized at the microvilli tips, or multiple chemistries with time-dependent levels of expression may be added. The versatility of the CDL-BIEM mobility calculation is that it can be extended to consider any of the following: more complex flowfields such as extensional flow or a recirculating flow, a cylindrical boundary, nonspherical corpuscles such as platelets or biconcave disks, periodic systems representing hundreds or thousands of cells, and finally, elastically deformable bodies that more closely resemble real cells. The paper presented here is the first step in a full simulation of adhesive phenomena in blood flow; we will address many of the above issues in papers to follow.

## APPENDIX

In this Appendix, we give the form of the lubrication forces generated by relative motion of two closely separated spheres. Derivation of these solutions can be found in Kim and Karilla (1991). Consider a sphere of radius $a$ and a second stationary sphere with radius $b = \beta a$, separated by a surface-to-surface distance $\epsilon a$. If the first sphere (A) is translating with velocity $U_A$ perpendicular to the line connecting their centers, the force and torque on sphere A are

$$\frac{F_x}{6\pi\mu a U_A} = -\frac{4\beta(2+\beta+2\beta^2)}{15(1+\beta)^3}\log(1/\epsilon) + A(\beta) - \frac{4(16-45\beta+58\beta^2-45\beta^3+16\beta^4)}{375(1+\beta)^4} \times \epsilon\log(1/\epsilon) + O(\epsilon), \tag{A1}$$

$$\frac{T_y}{8\pi\mu a^2 U_A} = \frac{\beta(4+\beta)}{10(1+\beta)^2}\log(1/\epsilon) + B(\beta) + \frac{(32-33\beta+83\beta^2+43\beta^3)}{250(1+\beta)^3} \times \epsilon\log(1/\epsilon) + O(\epsilon), \tag{A2}$$

where A($\beta$) and B($\beta$) are $O(1)$ terms found by matching with the outer solution. Similarly, if sphere A is rotating about the $y$-axis with angular velocity $\omega_A$, then the expressions for the resulting force and torque on sphere A become

$$\frac{F_x}{8\pi\mu a^2 \omega_A} = -\frac{\beta(4+\beta)}{10(1+\beta)^2}\log(1/\epsilon) + B(\beta) + \frac{(32-33\beta+83\beta^2+43\beta^3)}{250(1+\beta)^3} \times \epsilon\log(1/\epsilon) + O(\epsilon), \tag{A3}$$

$$\frac{T_y}{8\pi\mu a^3 \omega_A} = -\frac{2\beta}{5(1+\beta)}\log(1/\epsilon) + C(\beta) - \frac{2(8+6\beta+33\beta^2)}{125(1+\beta)^2}\epsilon\log(1/\epsilon) + O(\epsilon). \tag{A4}$$

The case of sphere A approaching the second sphere with velocity $U_A$ produces a stronger lubrication singularity, with the resulting force on sphere A equal to

$$\frac{F_z}{6\pi\mu a U_A} = -\frac{\beta^2}{(1+\beta)^2}\epsilon^{-1} - \frac{(1+7\beta+\beta^2)}{5(1+\beta)^3}\log(1/\epsilon) + \mathrm{K}(\beta) - \frac{(1+18\beta-29\beta^2+18\beta^3+\beta^4)}{21(1+\beta)^4}\epsilon\log(1/\epsilon) + O(\epsilon). \tag{A5}$$

The lubrication forces and torques produced by the close interaction between a sphere and a plane are a special case of the above relations (let $\beta \rightarrow \infty$), and can be obtained from the literature (Jeffrey, 1915; Brenner, 1961; Goldman et al., 1967a,b).

This work was funded by the National Institutes of Health (NIH), Grant No. HL18208, and an NIH National Research Service Award to M.K. (F32 HL10353). M.K. gratefully acknowledges the help of Dr. Stephen Rodgers for demonstrating the cell-free rolling technology.

## REFERENCES

Alon, R., D. A. Hammer, and T. A. Springer. 1995. Lifetime of the P-selectin–carbohydrate bond and its response to tensile force in hydrodynamic flow. *Nature.* 374:539–542.

Bell, G. I. 1978. Models for the specific adhesion of cells to cells. *Science.* 200:618–627.

Bell, G. I., M. Dembo, and P. Bongrand. 1984. Competition between non-specific repulsion and specific bonding. *Biophys. J.* 45:1051–1064.

Bevilacqua, M. P., R. M. Nelson, G. Mannori, and O. Cecconi. 1994. Endothelial–leukocyte adhesion molecules in human disease. *Annu. Rev. Med.* 45:361–378.

Bossis, G., A. Meunier, and J. D. Sherwood. 1991. Stokesian dynamics simulations of particle trajectories near a plane. *Phys. Fluids A.* 3:1853–1858.

Brady, J. F., and G. Bossis. 1988. Stokesian Dynamics. *Ann. Rev. Fluid Mech.* 20:111–157.

Brenner, H. 1961. The slow motion of a sphere through a viscous fluid towards a plane surface. *Chem. Eng. Sci.* 16:242–251.

Brunk, D. K., D. J. Goetz, and D. A. Hammer. 1996. Sialyl Lewis$^x$/E-selectin-mediated rolling in a cell-free system. *Biophys. J.* 71:2902–2907.

Brunk, D. K., and D. A. Hammer. 1997. Quantifying rolling adhesion with a cell-free assay: E-selectin and its carbohydrate ligands. *Biophys. J.* 72:2820–2833.

Bullard, D., E. Kunkel, H. Kubo, M. Hicks, I. Lorenzo, N. Doyle, C. Doerschuk, K. Ley, and A. Beaudet. 1996. Infectious susceptibility and severe deficiency of leukocyte rolling and recruitment in E-selectin and P-selectin double mutant mice. *J. Exp. Med.* 18:2329–2336.

Chang, K.-C. 1996. Adhesive dynamics simulation of receptor-mediated cell adhesion on surfaces under flow. Ph.D. thesis. Cornell University, Ithaca, NY.

Chang, K.-C., and D. A. Hammer. 1999. The forward rate of binding of surface-tethered reactants: effect of relative motion between two surfaces. *Biophys. J.* 76:1280–1292.

Chang, K.-C., and D. A. Hammer. 2000. Adhesive dynamics simulations of sialyl-Lewis$^x$/E-selectin-mediated rolling in a cell-free system. *Biophys. J.* 79:1891–1902.

Chang, K.-C., D. F. J. Tees, and D. A. Hammer. 2000. The state diagram for cell adhesion under flow: leukocyte rolling and firm adhesion. *Proc. Natl. Acad. Sci. U.S.A.* 97:11262–11267.

Damiano, E. R., J. Westheider, A. Tozeren, and K. Ley. 1996. Variation in the velocity, deformation, and adhesion energy density of leukocytes rolling within venules. *Circ. Res.* 79:1122–1130.

Dembo, M., D. C. Torney, K. Saxman, and D. A. Hammer. 1988. The reaction-limited kinetics of membrane-to-surface adhesion and detachment. *Proc. R. Soc. Lond. B. Biol. Sci.* 234:55–83.

Ebnet, K., and D. Vestweber. 1999. Molecular mechanisms that control leukocyte extravasation: the selectins and the chemokines. *Histochem. Cell Biol.* 112:1–23.

Evans, E., and K. Ritchie. 1997. Dynamic strength of molecular adhesion bonds. *Biophys. J.* 72:1541–1555.

Finger, E. B., K. D. Puri, R. Alon, M. B. Lawrence, U. H. von Andrian, and T. A. Springer. 1996. Adhesion through L-selectin requires a threshold hydrodynamic shear. *Nature.* 379:266–269.

Goetz, D. J., M. E. El-Sabban, B. U. Pauli, and D. A. Hammer. 1994. Dynamics of neutrophil rolling over stimulated endothelium in vitro. *Biophys. J.* 66:2202–2209.

Goldman, A. J., R. G. Cox, and H. Brenner. 1967a. Slow viscous motion of a sphere parallel to a plane wall. I. Motion through a quiescent fluid. *Chem. Eng. Sci.* 22:637–652.

Goldman, A. J., R. G. Cox, and H. Brenner. 1967b. Slow viscous motion of a sphere parallel to a plane wall. II. Couette flow. *Chem. Eng. Sci.* 22:653–660.

Goldsmith, H. L., and S. Spain. 1984. Margination of leukocytes in blood—flow through small tubes. *Microvasc. Res.* 27:204–222.

Greenberg, A. W., D. K. Brunk, and D. A. Hammer. 2000. Cell-free rolling mediated by L-selectin and sialyl Lewis$^x$ reveals the shear threshold effect. *Biophys. J.* 79:2391–2402.

Hammer, D. A., and S. M. Apte. 1992. Simulation of cell rolling and adhesion on surfaces in shear flow: general results and analysis of selectin-mediated neutrophil adhesion. *Biophys. J.* 62:35–57.

Higdon, J. J. L., and J. N. Viera. 2000. Colloidal Simulations with $O(N \ln N)$ Stokesian Dynamics. AIChE 2000 Annual Meeting, Los Angeles, California, Nov. 12–17, 2000.

Jeffrey, G. B. 1915. On the steady rotation of a solid of revolution in a viscous fluid. *Proc. Lond. Math. Soc.* 14:327–338.

Kim, S., and S. J. Karrila. 1991. Microhydrodynamics: Principles and Selected Applications. Butterworth-Heinemann, Stoneham, MA.

Kunkel, E. J., J. E. Chomas, and K. Ley. 1998. Role of primary and secondary capture for leukocyte accumulation in vivo. *Circ. Res.* 82:30–38.

Lasky, L. A. 1995. Selectin–carbohydrate interactions and the initiation of the inflammatory response. *Annu. Rev. Biochem.* 64:113–139.

Lawrence, M. B., and T. A. Springer. 1991. Leukocytes roll on a selectin at physiologic flow rates: distinction from and prerequisite for adhesion through integrins. *Cell.* 65:859–873.

Lipowsky, H. H., D. Riedel, and G. S. Shi. 1991. In vivo mechanical properties of leukocytes during adhesion to venular endothelium. *Biorheology.* 28:53–64.

Melder, R. J., J. Yuan, L. L. Munn, and R. K. Jain. 2000. Erythrocytes enhance lymphocyte rolling and arrest in Vivo. *Microvasc. Res.* 59:316–322.

Munn, L. L., R. J. Melder, and R. K. Jain. 1996. Role of erythrocytes in leukocyte–endothelial interactions: mathematical model and experimental validation. *Biophys. J.* 71:466–478.

Phan-Thien, N., D. Tullock, and S. Kim. 1992. Completed double layer in half-space: a boundary element method. *Comp. Mech.* 9:121–135.

Pozrikidis, C. 1999. A spectral-element method for particulate Stokes flow. *J. Comput. Phys.* 156:360–381.

Rodgers, S. D., R. T. Camphausen, and D. A. Hammer. 2000. Sialyl Lewis$^x$-mediated, PSGL-1-independent rolling adhesion on P-selectin. *Biophys. J.* 79:694–706.

Simon, S. I., Y. Hu, D. Vestweber, and C. W. Smith. 2000. Neutrophil tethering on E-selectin activates $\beta_2$ integrin binding to ICAM-1 through a mitogen-activated protein kinase signal transduction pathway. *J. Immunol.* 164:4348–4358.

Smith, M. J., E. L. Berg, and M. B. Lawrence. 1999. A direct comparison of selectin-mediated transient, adhesive events using high temporal resolution. *Biophys. J.* 77:3371–3383.

Takamura, K., H. L. Goldsmith, and S. G. Mason. 1981. The microrheology of colloidal dispersions. XII. Trajectories of orthokinetic pair-collisions of latex spheres in a simple electrolyte. *J. Colloid Interf. Sci.* 82:175–189.